PHYSICAL REVIEW B VOLUME 56, NUMBER 19 15 NOVEMBER 1997-I

Pattern formation during electropolishing

Vadim V. Yuzhakov, Hsueh-Chia Chang,* and Albert E. Miller
Department of Chemical Engineering, University of Notre Dame, Notre Dame, Indiana 46556

(Received 7 April 1997)

Using atomic force microscopy, we find that the surface morphology of a dissolving aluminum anode in a commercial electropolishing electrolyte can exhibit both highly regular and randomly packed stripe and hexagonal patterns with amplitudes of about 5 nm and wavelengths of 100 nm. The driving instability of this pattern formation phenomenon is proposed to be the preferential adsorption of polar or polarizable organic molecules on surface ridges where the contorted double layer produces a higher electric potential gradient. The enhanced relative coverage shields the anode and induces a smaller dissolution rate at the ridges. The instability is balanced by surface diffusion of the adsorbate to yield a length scale of $4\pi(D_s/k_d)^{1/2}$, where D_s is the surface diffusivity and k_d is the desorption coefficient of the adsorbate, which correlates well with the measured wavelength. A long-wavelength expansion of the double-layer field yields an interface evolution equation that reproduces all of the observed patterns. In particular, bifurcation analysis and numerical simulation yield a single voltage-dependent dimensionless parameter ξ that measures a balance between smoothing of adsorbate concentration by electric-field-dependent surface diffusion and fluctuation due to interfacial curvature and stretching. Randomly oriented stripes are favored at large ξ (low voltage), while random hills dominate at small ξ (high voltage) with perfectly periodic stripes and hexagonal hill patterns within a small window near $\xi=1$. These predictions are in qualitative and quantitative agreement with our measurements. [S0163-1829(97)04744-9]

INTRODUCTION

With the introduction of atomic force microscopy (AFM), the surface morphology of metal surfaces can now be examined at nanoscales. Not surprisingly, a myriad of patterns have been uncovered with very rich pattern formation dynamics. Surface structures on single-crystal electrodes have been shown[1] to change with applied voltage and adsorbate-induced mobility as surface atoms rearrange to form strikingly regular stripes and dots with amplitudes of 0.3 Å and wavelengths of 25 Å. Such stripe/dot patterns are also observed when surfactants self-assemble at solid-liquid interfaces.[2] These aggregates form micelle cylinders, hemicelles, and other patterns a few angstroms deep and about 10 nm long.

Most scrutiny of such patterns exploits the double-layer repulsion between the tip of the atomic force microscope and the sample. Such double layers appear on the electrode surface when one or two layers of polar water molecules[3] or solvated ions[4] are electrostatically packed against the electrode. This well-packed (Helmholtz) layer of oriented polar molecules or ions greatly reduces the transport of ions to the electrode interface such that the current through the layer can be small. As such, the layer functions as a molecular-size electrochemical capacitor between the anode surface proper and the closest packed anions. Due to the small separation, the capacitance can reach as high as 100 μF cm^{-2} by charging the electrode at a small current ($\sim$1 A/cm^2). At small applied voltage ($<$1 V), the potential drop $\Delta\psi_H$ across the Helmholtz layer is significant compared to the overall drop. Moreover, this drop $\Delta\psi_H$ can vary as the dissolution reaction proceeds. Any charge carried by the ion can either charge/discharge the electrochemical capacitor or be consumed in the dissolution reaction, which is usually assumed to be an activated process with an activation energy that depends on $\Delta\psi_H$.[5] When the capacitance dynamics is driven by these two parallel mechanisms, fronts and patterns can appear.[6] However, at the large applied voltage ($>$10 V) encountered in electropolishing, the packing is saturated and the total charge packed against a flat electrode is at its maximum value and it remains constant. As a result, $\Delta\psi_H$ remains constant and is much smaller than the total applied voltage. Moreover, under this diffusion-controlled condition of electropolishing, the average dissolution rate is equal exactly to the diffusion flux of water molecules or solvated ions, which participate in the dissolution reaction, outside the Helmholtz layer. In this diffusive layer outside the Helmholtz layer, the electric potential decays to the zero reference value of the electrolyte over a small distance of about 10–100 nm. Since the current is small, the flux of ions driven by both the electric potential and the concentration gradient must also be small. As such, the anion concentration decreases away from the anode while the cation concentration increases to counter the potential gradient. This quasisteady charge separation is usually described by the Poisson-Boltzmann distribution[7] such that charge at any position scales as $\sinh(\psi/\delta_E^2)$ or ψ/δ_E^2 for dilute electrolytes, where $\delta_E\sim$ 1–20 nm, the Debye thickness of the double layer measuring the characteristic length of decay for the potential in the diffusive layer. Consequently, a large electric field is induced at the interface between the Helmholtz and diffusive layers.

From AFM studies, it is now known that this large electric field introduced by the double layer can fundamentally affect the adsorption affinity of polar or polarizable organic adsorbates and ionic surfactants. Since the former can mobilize surface atoms and trigger surface reconstruction while surfactant aggregation and phase change are obviously sensitive to surfactant-electrode interaction, the observed patterns are extremely sensitive to the applied voltage that specifies the strength of the electric field at the double layer.

Electropolishing of metals to produce optically reflective surfaces is designed carefully such that only rough bumps on the electrode are dissolved away. This requires a slow dissolution process that reaches a maximum of about 1.5 $\mathrm{A/cm^2}$ at 70 V. Much of the resistance is traditionally attributed to the existence of a hydrodynamic diffusion boundary layer[8] of thickness δ_D. Since the ions must transport through this boundary layer before reacting, a slow transport would then yield a slow dissolution process. However, double layers must also exist during most electropolishing processes with such small currents. (Electropolishing conditions are quite similar to surface chemistry experiments with AFM detectable double layers.) This then offers additional resistance to ion transport, in series with the hydrodynamic diffusion boundary layer. In fact, it is quite possible that this double layer offers a resistance comparable to or larger than the hydrodynamic diffusive boundary layer. A slow dissolution rate is only achieved when the ion concentration and pH of the electrolyte are carefully controlled. These factors are known to affect δ_E as well as the dissolution chemistry and hence the ion transport rate to the anode. Because of the resistance of the double layers ($\delta_E \sim 10$ nm) on the anode and of the hydrodynamic diffusion boundary layers ($\delta_D \sim 1$ μm), the dissolution rate is controlled by the transport of ions[9] and not by the dissolution reaction, whose detailed microscopic mechanism remains unknown.[10,11] It is the transport through the hydrodynamic diffusion layer that preferentially dissolves macroscopic roughness with an amplitude in excess of 100 nm, approaching that of δ_D. Smaller roughness on the order of δ_E, however, would not be affected by the transport enhancement due to change in δ_D in light of the length scale separation $\delta_E/\delta_D \ll 1$. It is hence quite conceivable that optically reflective metals from electropolishing still possess irregularity of the amplitude δ_E or smaller. For roughness of this amplitude to ''self-assemble'' into regular patterns, however, there must exist an instability mechanism at the length scale of δ_E to preferentially select/amplify certain length scales.

In solidification processes, transport in the liquid phase to a maximum at the phase interface is enhanced either due to the reduction in δ_D for high Péclet transport or in diffusion length in globally diffusive transport.[12] As such, the unstable situation of a maximum growing faster than a minimum on the surface occurs and solidification processes have a rich spectrum of patterns driven by this instability. In dissolution or melting, however, the enhanced transport from a interfacial maximum serves to diminish its relative growth rate with respect to the minimum. Dissolution processes are then known to produce very smooth and stable interfaces. As a result, any pattern that appears at the δ_E level must be of chemical origin with a double layer playing a paramount role. They are also quite unexpected for a dissolution process, especially in electropolishing, which is supposed to yield a smooth surface.

As early as 1956, Welsh[13] reported observation of small-scale patterns on electropolished Al, but dismissed it as regular incoherence in the bulk grain boundary of the metal. We shall offer more direct evidence of stripe and dot (hexagon) patterns on polished Al. More importantly, we shall demonstrate strong correlation between the length scales (~ 100 nm) and patterns of these structures and the applied potential and hence disprove the theory that they are uncovered incoherence of the bulk grain boundaries. Instead, the strong voltage dependence suggests a double-layer driven instability mechanism is responsible for the surprising patterns. Our theoretical analysis will further support the proposed mechanism by providing an accurate prediction of the small voltage windows where regular stripes and hexagons can be observed.

I. EXPERIMENTS

Aluminum foil (Johnson Mattley) of 99.997% purity was used as the anode in a LECO EP-50 electropolisher apparatus (LECO is a commercial electropolisher vendor). The anode is a circular disk whose exposed diameter is 6 mm and is separated from the grade 304 stainless-steel cathode by 3 mm. The electrolyte flows between the anode and cathode such that the average liquid velocity is 0.1 m/sec. The electropolisher is maintained at a constant temperature of 15 °C by a coolant.

The Al coupons were first degreased with trichloroethylene and then electropolished in the LECO $L1$ electrolyte. The electrolyte consists of 70.0 vol % of ethanol $\mathrm{CH_3CH_2OH}$), 13.8 vol % of distilled water, 10.0 vol % of Butyl Cellusolve [or 2-butoxyethanol $\mathrm{CH_3(CH_2)_3OCH_2CH_2OH}$], and 6.2 vol % of perchloric acid ($\mathrm{HClO_4}$). The ethanol acts as a high-kinematic-viscosity and wetting solvent for the molecules/ions involved in the dissolution. The high viscosity ensures that the momentum boundary layer is thicker than that of the diffusion boundary layer on the disk such that the ion flux to the electrode is not affected by bulk turbulence and eddies, which can introduce large-scale nonuniformity. According to the bulk kinetics study of Vidal and West,[11] water molecules are the bulk acceptor molecules that provide the necessary ions to react with Al^{3+}, the aluminum ion released by the dissolving Al anode. The perchloric acid is to achieve the proper low pH to ensure that Al ionizes into Al^{3+} and does not form other ions or oxides in the anodization reaction. The perchloric acid ions act essentially as catalysts on the metal that release the Al^{3+} ions. (A Pourbaix diagram determining when Al^{3+} ions are formed can be found in Ref. 14). Since perchloric acid is a strong oxidizer, it can often oxidize violently at elevated temperatures. In addition to careful temperature control, Butyl Cellusolve is added as a stabilizer.

Both ethanol and Butyl Cellusolve are polar molecules with permanent dipoles. In fact, the stronger dipole on the Butyl Cellusolve lies on the branch that is identical to ethanol and hence has the same dipole moment. Moreover, the dipole moment of ethanol is numerically close to that of water [5.64×10^{-30} J/(V/m) compared to 6.17×10^{-30} J/(V/m), respectively]. For this reason, it is quite conceivable that the well-packed species near the electrode that produce the double-layer effect are not only the proposed water molecules[3] or solvated atoms,[4] but also the more abundant ethanol molecules. Solvated ions from dissociated water, perchloric acid, and Al^{3+} can also be present in the double layer. We shall not speculate on the chemical composition of the double layer but merely stipulate its presence in our

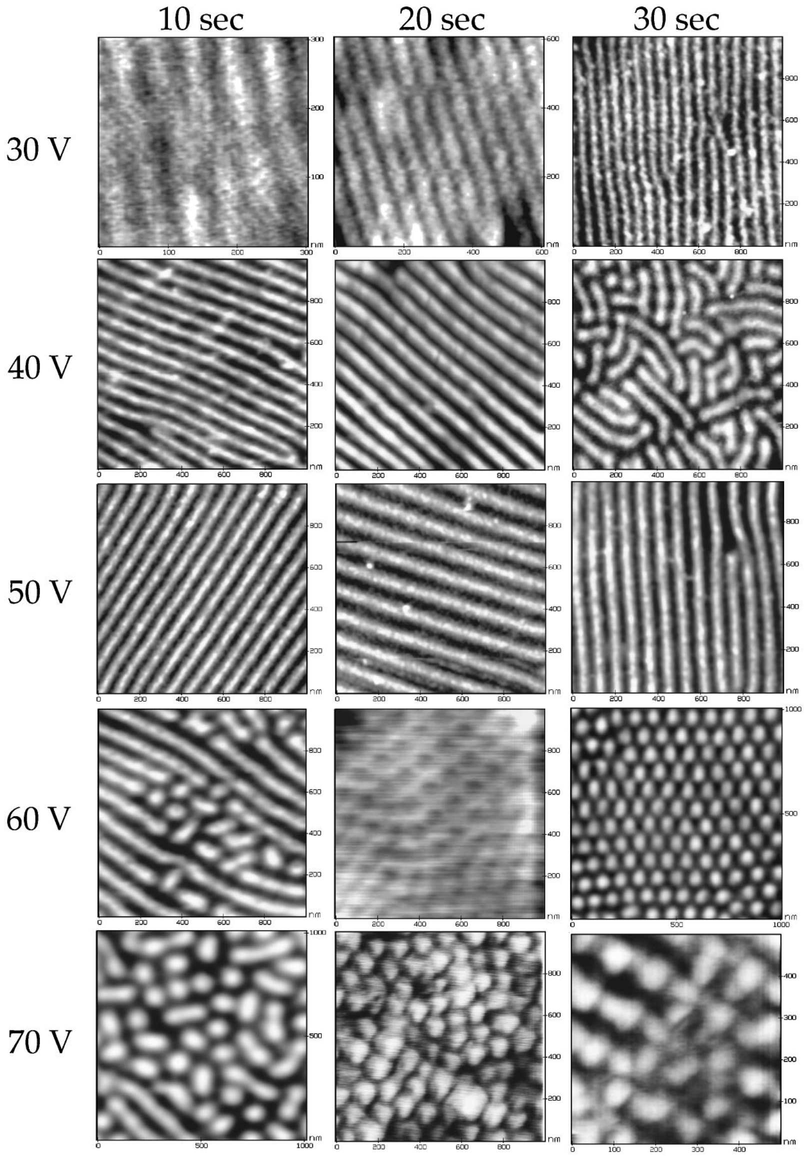

FIG. 1. Plethora of surface features that are produced on an aluminum surface by electropolishing in perchloric acid, Butyl Cellusolve, ethanol, and distilled water under various voltages and for various durations.

model. Nor can we detect any significant hydrophobic or hydrophilic parts in any of our species that will allow them to aggregate and form surface micellar structures such as surfactants or lipids.

We find our patterns to be insensitive to the electrolyte flow velocity, suggesting that δ_D does not play a role. They are, however, strong functions of the applied voltage, suggesting the paramount role of the double layer. We have yet to alter the composition of the electrolyte. Since this may change the reaction chemistry as well as double-layer thickness, the effect of electrolyte composition requires more detailed knowledge about the dissolution kinetics than is currently available. We hence use the same electrolyte in all experiments and vary only the voltage and the polishing time. The dissolution chemistry then presents itself as an unknown but constant factor in our model, which is a physical model describing how interfacial curvature affects the local electric field and in turn the local dissolution rate.

AFM examination of the samples prior to electropolishing reveals a rough surface with random nonuniformities greater than 50 nm peak to valley over a 6-μm square scan area. Electropolishing this surface dramatically reduces this height range for all applied voltages studied to less than 3 nm after polishing. Persistent regular patterns of this latter height survive, however. As shown in the AFM images in Fig. 1, the stripe structure appears first for any applied voltage but after a short transition time it may evolve into another structure. These asymptotic structures are usually established after 30 sec from the beginning of electropolishing. Representative top-view AFM images of the final surface structures observed for each of the electropolishing voltages examined are presented in Fig. 2. It can be seen from this figure that there exist four distinctly different types of final surface structures: random stripes for low voltage, regular stripes and regular hexagons for intermediate voltage, and random hills (which we shall refer to as random hexagons) for high voltage.

A two-dimensional spatial Fourier transform of the hexagonal pattern at 60 V in Fig. 3 demonstrates the extreme periodicity of this pattern. Amplitudes of the surface structures were measured with precision and they were found to

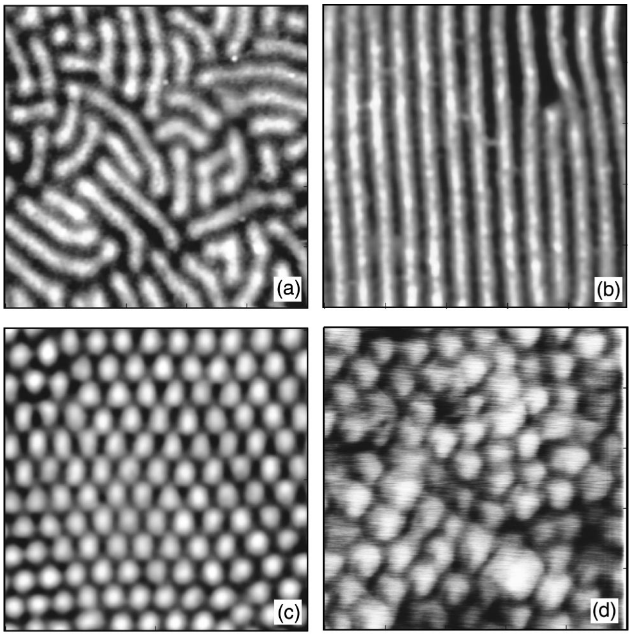

FIG. 2. Four typical patterns on the electropolished aluminum obtained for the applied voltage of (a) 40 V, random stripe pattern; (b) 50 V, regular stripe pattern; (c) 60 V, regular hexagon pattern; and (d) 70 V, random hills.

be in the range of 1–5 nm with a nonmonotonic dependence on voltage. However, the wavelengths are two orders of magnitude larger and can also be measured with great precision. They are observed to increase monotonically with respect to applied voltage as seen in Fig. 4.

II. MODEL

The characteristic amplitude of the observed pattern is of the order of δ_E. To obtain an instability mechanism, any variation of the anode from the planar geometry must be amplified by the double layer such that a maximum (ridge) on the electrode dissolves slower and a minimum (valley) dissolves faster. Such variations can distort the electric field within the diffusive layer and this must be how interfacial distortion transmits the initial disturbance to subsequent dissolution dynamics. Due to the high voltage with saturated packing, the potential drop $\Delta\psi_H$ within the Helmholtz layer remains constant and is negligible compared to the total applied voltage. Also, since the Helmholtz layer is thin compared to δ_E and the characteristic wavelength of the patterns, $\Delta\psi_H$ remains constant over the entire patterned surface during dissolution. Pattern formation is then driven only by spatial and temporal variations of the field in the outside diffusive layer. For the dilute electrolyte used, we can use the Debye-Hückel approximation in the Poisson equation that describes the potential field in the diffusive layer of the double layer,

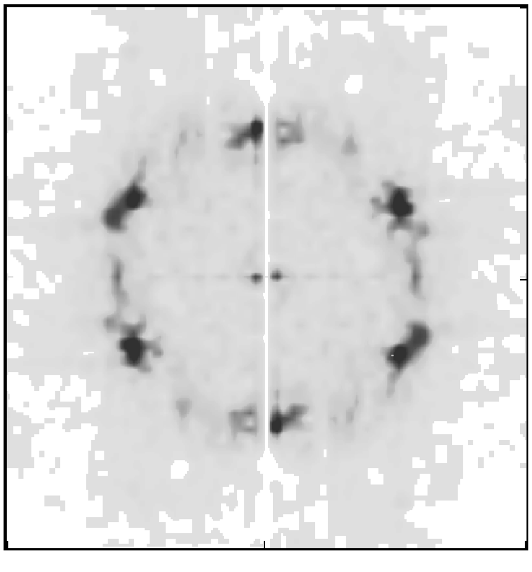

FIG. 3. Image of the first 47×47 modes of the two-dimensional Fourier spectrum for the AFM image of the $3\times3\ \mu\text{m}^2$ aluminum surface electropolished during 30 sec at 60 V.

$$\nabla_{\text{III}}^2\psi=\frac{\psi}{\delta_E^2},$$
$$\psi|_{z=h}=\psi_s, \tag{1}$$
$$\psi|_{z\to\infty}=0,$$

where, neglecting $\Delta\psi_H$, ψ_s is the potential at the anode relative to the bulk electrolyte, which has a constant potential set to zero (the potential gradient in the bulk electrolyte is negligible relative to the large potential gradient in the diffusive layer), and h is the interfacial position measured from the mean flat position. The term on the right-hand side of Eq. (1) represents the charge distribution and is proportional to ψ. For a flat interface $h=0$, the solution to Eq. (1) is simply

$$\psi_0=\psi_s\exp\left(-\frac{z}{\delta_E}\right), \tag{2}$$

which yields an electric field on the metal of

$$E_0=-\frac{d\psi}{dz}\bigg|_{z=0}=\frac{\psi_s}{\delta_E}. \tag{3}$$

(Since the Helmholtz layer is only a few angstroms and it is much smaller than δ_E, we have omitted it in the analysis.) Since the amplitude of the patterns is much smaller than the wavelength, we carry out a long-wavelength expansion of Eq. (1) in the Appendix to obtain a relationship between the electric field at the anode interface and the interfacial shape h,

$$E=-\frac{d\psi}{dn}\bigg|_{z=h}\approx E_0+E_1, \tag{4}$$

where d/dn is the normal gradient and the deviation electric field $E_1\ll E_0$ relative to the planar case is

$$E_1=-\frac{E_0}{2}[(\nabla h)^2+\delta_E\nabla^2 h], \tag{5}$$

where ∇, unlike ∇_{III} in Eq. (1), is the two-dimensional Laplace operator. It is hence clear that E_1/E_0 is of the order $(h/\ell)^2$ or $(\delta_E/\ell)^2$, where ℓ is the characteristic wavelength. As is observed, this long-wavelength parameter is small and of order 10^{-2}–10^{-1}; this justifies a long-

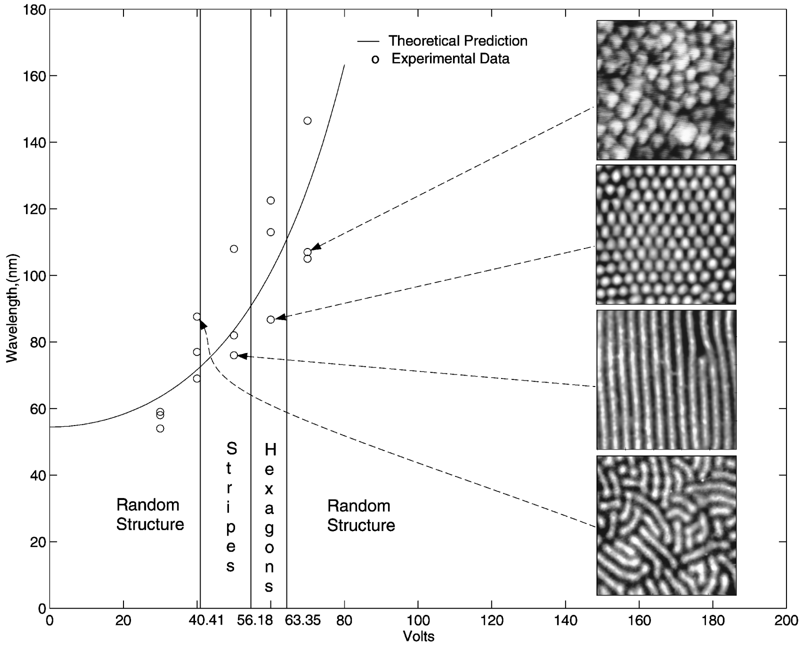

FIG. 4. Measured wavelength of the stripe and hexagonal patterns as a function of the applied voltage U. The solid curve and lines are the theoretical predictions; typical AFM images at 30 sec are also shown.

wavelength expansion to simplify E in the double layer and the subsequent derivation of a long-wavelength evolution equation for the anode interface. We shall use subscript or superscript 0 to denote the planar zero order state and 1 to denote the next-order correction that introduces interfacial curvatures.

The first term in Eq. (5) represents the ''stretching'' or ''tension'' term, which describes how the interface lengthens at the nodes. This stretched interface hence decreases the local potential gradient (field) due to the larger interfacial area. The second term is the curvature term which describes how a point on the anode ''sees'' the surface around it. If this point is at a maximum ($\nabla^2 h<0$), the receding surface around it enhances the field gradient. The opposite is true at a minimum where the gradient is reduced by the protruding surface around it.

There are several possible ways this slightly distorted electric field can affect the local dissolution rate. It is known[15] that the dissolution rate K_r depends on the anode electric field in the usual threshold Arrhenius form, known as the Tafel dependence,

$$K_r = K_r^* \exp\left(\frac{\beta_r E}{k_B T}\right),$$

where β_r is a proportionality coefficient that is typically of the order of 10^{-31} J/(V/m) for most metal anodes.[18] The preexponential factor K_r^* denotes the fieldless dissolution rate, which contains the weak dependence on bulk mass transport through the diffusion boundary layer δ_D and the stronger dependence on electrolyte composition, which can change the dissolution chemistry. It is a nominal fieldless limit of the dissolution rate since the dissolution chemistry can disappear entirely when no voltage is applied. We have instead assumed that the pertinent chemistry remains in place for the entire range of voltages. We are unable to detect any pattern, for example, at zero voltage in Fig. 4. Nevertheless, the extrapolation of the data to zero voltage represents this nominal limit that we shall use an asterisk to denote.

The dependence on voltage, however, is entirely in the activation energy. The rationale is that the dissolution reaction evolves through a bottleneck of ionic or polar transition state whose energy, relative to the undissolved anode, is proportional to the electric field. We can then carry out a long-wavelength expansion of the dissolution rate $K_r \approx K_r^0 + K_r^1$ to see how the deviation field E_1 affects it, how local tension and curvature affects dissolution. Due to the exponential dependence on field, we find as in all subsequent expansions of field-dependent rates that K_r^1 is proportional to K_r^0,

$$\frac{K_r^1}{K_r^0} \approx \frac{K_r - K_r^1}{K_r^0} \approx \frac{\beta_r}{k_B T} E_1 + \frac{1}{2}\left(\frac{\beta_r}{k_B T}\right)^2 E_1^2, \tag{6}$$

where we have carried out the expansion to second order in E_1. It is then clear that the maximum with a positive E_1 would have a higher dissolution rate, a stable negative feedback scenario.

Double layers are also known to induce phase changes in self-aggregating surfactants such that cylindrical and hemispherical surface micelles can form. If the increased field ($E_1>0$) at a maximum can precipitate such a transition, the micelles can shield the maximum from further dissolution. However, such micelles require surfactants that can interact among themselves attractively to self-assemble. We find no evidence of such surfactant features in the chemical species present. In particular, Butyl Cellusolve, the most likely candidate, does not have a significant hydrophobic tail that can favor a micelle aggregation to shield the tails from water. The fact that stripes precede all other patterns (Fig. 1) also suggests that if a surface phase transition is driving the pattern formation process, the micelles need to break up intermittently along the ridge after they have aggregated to produce the ridges. This is a very unlikely scenario and the length scales[2] reported for such micelle structures are also an order of magnitude smaller than our patterns. We hence dismiss surfactant aggregation as the cause of our patterns.

However, adsorbates do not have to form surface micelles to affect dissolution adversely. Adsorbed organic molecules can change the energy of the surface metal atoms on an electrode and cause small-scale (25 Å wavelength and 1 atom in amplitude) atomic rearrangement.[1] The same adsorbate-metal interaction in the form of either electrostatic adsorption or chemisorption can also stabilize the surface atom and reduce its dissolution rate. The adsorbed organic molecule can further physically or chemically shield the surface to reduce the transport rate of the ions involved in the dissolution reaction. If such shielding molecules adsorb on the maxima with higher electric field ($E_1>0$) more readily than the minima with negative E_1, the necessary positive feedback is then available to provide a instability mechanism. This is more reasonable than aggregation of surfactants since adsorption and desorption occur more readily. These shielding molecules can even be the same ones that pack the surface to produce the double layer. Enhanced packing, if the packing species are not involved in the dissolution process, could reduce the dissolution rate by suppressing the ion flux. They must, however, be polar or polarizable molecules such that their adsorption rate is enhanced by the electric field.

In our electrolyte, water, ethanol, and Butyl Cellusolve are all possible candidates for the shielding molecule. Ethanol is, however, in abundance and they can saturate the surface such that small variations in E would not produce a significant variation in ethanol coverage. Water by itself or after ionization is supplying the reactant for dissolution; it is hence unlikely that enhanced water coverage can reduce reaction. It is then possible that it is the Butyl Cellusolve that is playing the role of the shielding molecule. A second possible scenario is that water can appear within complexes of solvated ions that have been speculated to be the packing species for the double layer.[1] Such symmetric polar complexes have fewer degrees of freedom than water, ethanol, or Butyl Cellusolve and hence can reach the anode more readily. Water molecules in such complexes can also be chemically stable and hence do not participate in the dissolution reaction. In this scenario, it can be the favorable packing of solvated ion complexes at the maxima that reduces the dissolution. Yet another possibility with a solvated-ion Helmholtz layer is that ethanol, Butyl Cellusolve, or even water molecules can compete with the solvated ions for the metal surface. If they succeed, the packing will have defects at locations where these molecules are either electrostatically adsorbed or site specifically chemisorbed. Chemisorption of these shielding molecules can stabilize surface Al atoms against dissolution. The short hydrophobic tail of ethanol and Butyl Cellusolve can also repel any solvated ion, such as OH^-, and hence reduce its flux to the surface to participate in the dissolution. Our suspicion is that Ethanol and/or Butyl Cellusolve are the most likely shielding molecules that can reduce ion flux and/or stabilize surface Al atoms. However, like identifying the packing species for the double layer, the exact identity of the shielding molecule(s) and how it reduces the local dissolution rate are a formidable kinetics problem that we shall undertake in the future.

It is quite apparent and reasonable, however, that such a molecule (or molecules) does exist and we shall model its effect without specifying its identity. To produce a length scale selection process and explain the appearance of such regular structures from an irregular surface, we must also introduce a short-wavelength cutoff mechanism to couple with the long-wavelength instability. While the enhanced dissolution rate is a stabilizing mechanism, it occurs at large wavelengths and at the same order as the long-wavelength shielding instability mechanism. The only short-wavelength cutoff possible is surface diffusion, as in other interfacial pattern evolution.[16] Hence the fractional surface coverage of the shielding molecule can be described by the quasisteady equation

$$D_s(E)\nabla^2\theta+k_a(E)-k_d(E)\theta=0. \tag{7}$$

The adsorption rate k_a is a function of the electrolyte composition, but since the composition does not vary in time, we do not consider it explicitly. It can also be a function of the diffusion boundary layer δ_D, but we find such a dependence weak. We have also assumed the coverage is small such that the adsorption rate is independent of θ. The desorption rate, however, must be a function of θ. Expanding about the planar case again and imposing the natural ordering $k_a-k_a^0=k_a^1\sim\theta_1$ such that the variation in the coverage θ is proportional to the variation in k_a, we obtain to order θ_1

$$D_s^0\nabla^2\theta_1+k_a^1-k_d^0\theta_1=0. \tag{8}$$

Note that correction to the diffusivity and desorption rate constants due to deviation from the planar geometry is unimportant. The adsorption rate of an organic molecule in competition with another one has a field-dependent activation energy that is proportional to the difference in their permanent and induced dipole moments.[17] Since all three polar molecules, water, ethanol, and Butyl Cellusolve, have roughly the same permanent dipoles, we assume that the adsorption rate of the shielding molecule is dependent only on the difference in its polarizability relative to the others, the relative polarizability,

$$k_a=k_a^*\exp\left(\frac{\alpha E^2}{2k_BT}\right), \tag{9}$$

where α is the difference in effective polarizability.

An effective α can be obtained by using the Debye-Langevin equation $\alpha=\alpha_0+P^2/3k_BT$, which contains both the difference in permanent dipole moments P and the difference in polarizabilities α_0. Since P is about 3×10^{-31} J/(V/m) [the dipole moments of water and ethanol are 6.17 $\times10^{-30}$ J/(V/m) and 5.64×10^{-30} J/(V/m), respectively], the difference in the permanent dipoles does not play a role compared to the difference in the polarizabilities, which is $\alpha_0\approx4.7\times10^{-40}$ J/(V/m)^2 for water and ethanol.

Expanding k_a about E_0 to obtain k_a^1 to $O(E_1^2)$, we obtain

$$k_a^1=\frac{\alpha E_0}{k_BT}k_a^0E_1+\frac{1}{2}\frac{\alpha}{k_BT}\left(\frac{\alpha E_0^2}{k_BT}+1\right)k_a^0E_1^2.$$

Substituting this into Eqs. (5) and (8), one obtains

$$\left(\frac{D_s^0}{k_d^0}\right)\nabla^2\theta-\theta=B_1\left[(\nabla h)^2+\delta_E\nabla^2 h-\frac{\delta_E^2}{4}\left(\frac{\alpha E_0^2}{k_BT}+1\right)(\nabla^2 h)^2\right] \tag{10}$$

by omitting terms higher order than $O(h^2)$. This restricts our theory to small-amplitude, nearly sinusoidal shapes with weak nonlinear effects. Since we can obtain an accurate profile of our observed patterns, this seems like a good approximation considering the measured small amplitude relative to the wavelength. This weakly nonlinear approximation greatly simplifies our analysis and the same simplification in Eq. (10) describes how the coverage of shielding molecule changes due to variation of the interfacial position from the planar geometry. The first term on the right-hand side indicates that the coverage will decrease at the nodes due to the decreased field from interface stretching. The second term indicates that the coverage increases (decreases) at a maximum (minimum) due to curvature-enhanced (reduced) field. The last term is a higher-order curvature term that increases the coverage at both the maxima and the minima. The dimensionless parameter B_1 represents the sensitivity of the adsorption rate to field changes, a normalized activation energy,

$$B_1=K_a^0(E_0)\frac{\alpha E_0^2}{k_BT}, \tag{11}$$

where $K_a^0=k_a^0/k_d^0$ is the equilibrium constant for the adsorption-desorption process.

It is now a matter of relating the coverage of the shielding molecule to the dissolution rate. The Tafel expression (5) for dissolution rate assumes a planar equilibrium coverage θ_0. Hence the deviation dissolution rate from the planar case is

$$\frac{\partial h}{\partial t}=K_r^0\theta_1-K_r^1. \tag{12}$$

The first term is obviously due to molecular shielding, while the second term is the change in the dissolution rate due to the unshielded field variations on a nonplanar anode in Eq. (6). Combining Eq. (6) with the field-interface correlation (5), one gets

$$\frac{K_r^1}{K_r^0}=-B_2\left[(\nabla h)^2+\delta_E\nabla^2 h-\frac{B_2}{2}(\delta_E\nabla^2 h)^2\right], \tag{13}$$

where again we have neglected terms of $O(h^3)$ and higher and the parameter B_2 measures the sensitivity of unshielded dissolution to field changes: It is simply the normalized activation energy

$$B_2=\frac{\beta_r E_0}{2k_BT}. \tag{14}$$

For most dissolution reactions, B_2 is a very small parameter. The estimated values for Al in most electrolytes range 0.05–0.15.[18] Hence we shall safely omit the third term on the right-hand side of Eq. (13). The high-order nonlinear mechanism arises solely from the shielding mechanism described in Eq. (10).

Inserting the coverage-interface correlation (10) and the dissolution-interface correlation of Eq. (13) into the evolution equation (14), we obtain the final weakly nonlinear evolution equation

$$\frac{\partial h}{\partial t}-\left(\frac{D_s^0}{k_d^0}\right)\nabla^2\frac{\partial h}{\partial t}=K_r^0B_1\left[-(1-\nu)(\nabla h)^2-(1-\nu)\delta_E\nabla^2 h-\nu\left(\frac{D_s^0}{k_d^0}\right)\delta_E\nabla^4 h-\nu\left(\frac{D_s^0}{k_d^0}\right)\nabla^2(\nabla h)^2+\frac{\delta_E^2}{4}\left(\frac{\alpha E_0^2}{k_BT}+1\right)(\nabla^2 h)^2\right], \tag{15}$$

where $\nu=B_2/B_1$ measures the ratio of the activation energies for the two key processes: dissolution and adsorption. Using the scalings

$$t=\frac{\nu(D_s^0/k_d^0)}{K_r^0B_1(1-\nu)^2\delta_E}\tau,$$

$$(x,y)=\left(\frac{\nu}{1-\nu}\right)^{1/2}\left(\frac{D_s^0}{k_d^0}\right)^{1/2}(X,Y),$$

$$h=\delta_E H,$$

we obtain a dimensionless, weakly nonlinear evolution equation with only two parameters

$$H_\tau-\frac{(1-\nu)}{\nu}\nabla^2 H_\tau=-(\nabla H)^2-\nabla^2 H-\nabla^4 H-\nabla^2(\nabla H)^2+2\xi(\nabla^2 H)^2, \tag{16}$$

where

$$\xi=\frac{\delta_E^2}{8\nu}\left(\frac{k_d^0}{D_s^0}\right)\left(\frac{\alpha E_0^2}{k_BT}+1\right) \tag{17}$$

contains two ratios. The parameter $(D_s^0/k_d^0)^{1/2}$ represents the diffusion length on a planar anode for the shielding molecule over its lifetime. Hence $\delta_E^2(k_d^0/D_s^0)$ represents the squared ratio of the double-layer thickness to the diffusion length. More accurately, ξ measures the coupling between diffusion and interface curvature and stretching as we shall demonstrate subsequently. The parameter $\nu=B_2/B_1$, as mentioned earlier, represents the ratio of the activation energies of the stabilizing dissolution rate to that of the destabilizing adsorption. The evolution equation (16) contains terms similar to those in the Kardar-Parisi-Zhang equation[16] (and its extension to include surface diffusion[19]) for interfacial evolution of epitaxial films. However, field variation (due to interfacial curvature and stretching) affects the activation energies of both the adsorption of shielding molecules and the dissolution rate, with the former having the higher sensitivity to ensure an instability mechanism. As a result, we obtain a unique $\nabla^2 H_\tau$ due to the coupling between diffusion and shielding. We also obtain higher-order terms such as $\nabla^2(\nabla H)^2$ and $(\nabla^2 H)^2$ from the higher-order field dependence of adsorption and dissolution processes and from higher-order diffusion-adsorption coupling. Such higher-order terms are necessary to allow a quantitative prediction of the various patterns appearing at different voltage. Without higher-order terms, we would only be able to predict the critical voltage for pattern formation, but not how the patterns depend on the voltage.

One observation can already be made. Since Eq. (16) is invariant to $(X,Y)\mapsto(-X,-Y)$, we expect all one-dimensional stripe patterns to be symmetric about the maxima and each hill in the two-dimensional hexagonal patterns to be nearly radially symmetric. This arises because the stretching at the nodes is independent of the direction of the slope. All slopes of the same amplitude would have identical field deviation from the mean and hence dissolve at the same rate. If the dissolution mechanism dominates $(\nu>1)$, the nodes will grow and if the shielding mechanism dominates $(\nu<1)$, the nodes will dissolve. We hence expect both the stripe and hill patterns that appear for the latter case to have sharper crests due to this enhanced symmetric dissolution of the nodes. Another significant observation concerns the higher-order $\nabla^2(\nabla H)^2$ and $(\nabla^2 H)^2$ terms that dictate a second-order transition. In particular, they determine whether stripes will break into hexagonal hills or remain as stripes. Since the evolution of well-developed stripes involves dissolution of their ridges where H_X vanishes and $(H_Y)^2$ is of the same magnitude at the disturbance maxima and minima along the ridge (assuming the ridges line up in the Y direction), the $(\nabla H)^2$ term does not participate and only the two higher-order nonlinear terms are involved. All linear terms are also ineffective for these developed stripes. In the evolution equation, $-\nabla^2(\nabla H)^2$ produces a pertinent $-2(\nabla^2 H)^2$ term at any maximum to compete with the $2\xi(\nabla^2 H)^2$ term. The first promotes ridge dissolution, while the second favors ridge growth. One hence expects stripes to dominate at large ξ and expects them to break up into hills at smaller ξ. A simple physical view of this is to notice that a ridge would only dissolve at certain positions if preferential dissolution at the nodes breaks the symmetry between the maxima and the minima along the ridge such that the latter has a lower curvature, smaller adsorption, and higher dissolution. This is favored by the $-\nabla^2(\nabla H)^2$ term when adsorption is more field sensitive than dissolution: The reduced field at the stretched nodes actually promotes dissolution.

The large-time dynamics governing reorientation of stripes and self-assembly of hills is also governed by these two terms. From the previous arguments, we expect hills to connect into irregular stripes at large ξ and stripes to break up into random hills at small ξ. It is only when ξ is close to unity, when these two opposing forces balance, that regular stripe and hexagonal hill patterns can be established. We hence expect the windows of perfectly regular stripe and hexagonal patterns to appear near $\xi=1$. The $(\nabla^2 H)^2$ term comes from the second-order field dependence in dissolution and adsorption and is explicitly obtained by squaring the curvature term $\nabla^2 h$ in the perturbation field E_1 in Eq. (5) for both dissolution (6) and adsorption (10). The $\nabla^2(\nabla H)^2$ term, on the other hand, comes from a coupled effect between diffusion and stretching $[(\nabla h)^2$ in Eq. (5)] on the induced coverage variation of the shielding molecule. The first term appears in any second-order curvature-driven dynamics, while the second term is unique to interfacial dynamics involving a coupling between surface diffusion and interfacial stretching. Both terms render the developed patterns rigid such that the pattern dynamics do not evolve indefinitely and seem to reach steady patterns after some transients. In the current context, this coupling is offered by the double-layer electric field that is affected by stretching and in turn affects the diffusing shielding molecule. It is a unique physical interfacial dynamics offered by electropolishing.

III. ANALYSIS AND SIMULATION

It is more apparent from the unnormalized evolution equation (15) that the planar geometry is linearly unstable if the adsorption rate is more sensitive to the electric field than the dissolution rate $\nu<1$. For the linearized scaled version (16), a normal mode $H\sim\exp[\lambda\tau+\mathrm{i}(kX+lY)]$ expansion yields the growth rate

$$\lambda=\frac{q^2-q^4}{1+\dfrac{(1-\nu)}{\nu}q^2}, \tag{18}$$

where $q^2=k^2+l^2$ is the generalized wave number. All Fourier modes with wave numbers (k,l) within the circle

$$k^2+l^2=1 \tag{19}$$

are hence unstable with the maximum growth rate at

$$q_m^2=k_m^2+l_m^2=\frac{\sqrt{\nu}}{1+\sqrt{\nu}}. \tag{20}$$

Our bifurcation analysis will first focus on the stripe and hexagonal patterns, which, as shown from the spatial Fourier transform in Fig. 3, consist of discrete Fourier modes within the unstable circle. Since stripes and hexagonal hills appear within a small window of the applied voltage while patterns outside resemble irregular stripes and hexagons, as seen in Fig. 4, the selected pattern over the entire range of voltage is expected to be determined by weakly nonlinear interaction between these two basic patterns. Both patterns can be represented by the discrete modes within the unstable band shown in Fig. 5, where we have chosen six discrete fastest growing modes along the circle described by Eq. (20). The symmetry of these discrete points in the wave-number space reflects the hexagonal symmetry. The stripes consist of any two of the six, while the hexagonal hills result from a linear combination of all six modes (or three complex modes). This signature pattern of the hexagon is also seen in Fig. 3.

We hence expand $H(X,Y,\tau)$ of Eq. (16) by these three active (master) complex modes, their passive (stable) overtone, and any other passive modes in the wave-number space of Fig. 5 that satisfies the resonance condition with the above modes

$$\mathbf{k}_p\pm\mathbf{k}_q\pm\mathbf{k}_r=0, \tag{21}$$

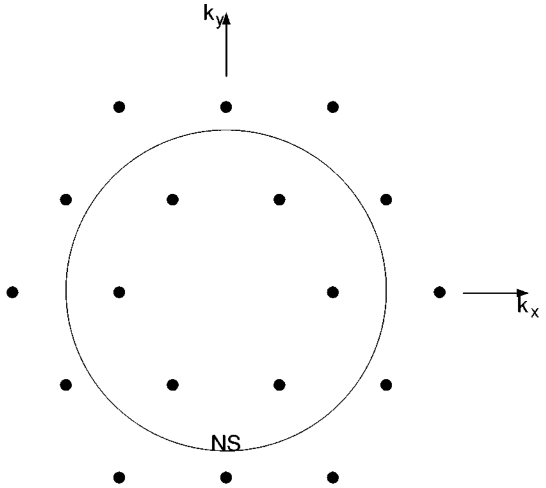

FIG. 5. Modes used in the representation of the relative deviation H for nonlinear analysis of pattern selection. The area within the neutral stability circle represents the region of active modes; the other area is the region of passive modes.

where $\mathbf{k}=(k,l)$ is the wave-number vector. A total of 9 complex modes, three active and six passive, are used as seen in Fig. 5. The expansion then becomes

$$H(\mathbf{r},t)=\sum_{j=1}^{3}\{W_j\exp(i\mathbf{k}_j\cdot\mathbf{r})+V_j\exp(2i\mathbf{k}_j\cdot\mathbf{r})+\hat{V}_j\exp[i(\mathbf{k}_j-\mathbf{k}_{j+1})\cdot\mathbf{r}]\},\tag{22}$$

where $\mathbf{r}=(X,Y)$, $|\mathbf{k}_j|=q_m$ of (20), W_j, V_j, and $\hat{V}_j$ are the complex amplitudes of the unstable master modes, their overtones and the other resonant modes, respectively.

By substituting Eq. (22) into the interfacial evolution equation (16) and collecting terms corresponding to the same Fourier mode, we then obtain nine coupled amplitude equations for all the modes. However, at large time, the dynamics is dominated by the active modes with the passive modes slaving to the dominant dynamics of these active modes. The ''adiabatic invariance'' describing this slaving principle can be derived explicitly using center manifold projection.[20–22] We omit the tedious algebra here and simply present the resulting set of three couple complex amplitude equations for the three active modes. One of them is

$$\frac{\partial W_1}{\partial\tau}=\frac{16}{81}W_1+\gamma_1W_2^*W_3^*-\gamma_2|W_1|^2W_1-\gamma_3(|W_2|^2+|W_3|^2)W_1.\tag{23}$$

Due to the hexagonal symmetry, the other amplitude equations for W_2 and W_3 can be obtained from Eq. (23) by obvious permutation of indices.

The coupling coefficients γ_j are functions of ν and ξ. As seen earlier, the parameter ν, representing the ratio of the sensitivity of the dissolution and adsorption processes to electric-field variation, must be less than unity for patterns to appear. We shall show in Sec. IV that, for reasonable parameter values for the electropolishing of Al, the values of ν remain relatively constant at around 0.5 for the important voltage range of $U\in$ (20 V, 80 V). This observation allows us to fix ν and vary only ξ in our analysis and numerical simulations. In fact, since the maximum-growing wave number (20) and its growth rate are functions only of $\nu^{1/2}$, we shall choose $\nu=0.64$ for convenience. The actual dependence of ν on E_0 is

$$\nu(E_0)=\frac{\beta_r}{2\alpha E_0K_a^0(E_0)}$$

and hence this simplification may not be permissible for other system with a more sensitive adsorption rate dependence on the field.

With $\nu=0.64$, the nonlinear terms $(\nabla H)^2$, $\nabla^2(\nabla H)^2$, and $(\nabla^2H)^2$ of the evolution equation yield the following simple ξ dependence for the coupling coefficients γ_j:

$$\gamma_1=\frac{4}{81}(16\xi-17),$$

which represents quadratic coupling between active modes

$$\gamma_2=\frac{8}{891}(16\xi-5)(7-8\xi),$$

$$\gamma_3=\frac{7}{621}(16\xi-9)(15-16\xi),$$

which represent the degree of cubic coupling between active modes.

After transformation to the polar coordinate system such that $W_j\equiv R_j\exp(i\varphi_j)$, Eq. (19) yields a system of equations for the real part of the amplitudes and the sum of the phases $\Phi=\varphi_1+\varphi_2+\varphi_3$ for the active modes:

$$\frac{\partial R_1}{\partial\tau}=\frac{16}{81}R_1+\gamma_1R_2R_3\cos\Phi-\gamma_2R_1^3-\gamma_3(R_2^2+R_3^2)R_1,$$

$$\frac{\partial R_2}{\partial\tau}=\frac{16}{81}R_2+\gamma_1R_3R_1\cos\Phi-\gamma_2R_2^3-\gamma_3(R_3^2+R_1^2)R_2,\tag{24}$$

$$\frac{\partial R_3}{\partial\tau}=\frac{16}{81}R_3+\gamma_1R_1R_2\cos\Phi-\gamma_2R_3^3-\gamma_3(R_1^2+R_2^2)R_3,$$

$$\frac{\partial\Phi}{\partial\tau}=-\gamma_1\frac{R_1^2R_2^2+R_2^2R_3^2+R_3^2R_1^2}{R_1R_2R_3}\sin\Phi.$$

Thus the phase Φ relaxes monotonically to 0 when $\gamma_1>0$ and relaxes monotonically to π when $\gamma_1<0$. In both cases, $\gamma_1\cos\Phi=|\gamma_1|$ and only the amplitude dynamics is important at long times,

$$\frac{\partial R_1}{\partial\tau}=\frac{16}{81}R_1+|\gamma_1|R_2R_3-\gamma_2R_1^3-\gamma_3(R_2^2+R_3^2)R_1,$$

$$\frac{\partial R_2}{\partial\tau}=\frac{16}{81}R_2+|\gamma_1|R_3R_1-\gamma_2R_2^3-\gamma_3(R_3^2+R_1^2)R_2,$$

$$\frac{\partial R_3}{\partial\tau}=\frac{16}{81}R_3+|\gamma_1|R_1R_2-\gamma_2R_3^3-\gamma_3(R_1^2+R_2^2)R_3.\tag{25}$$

This system of equations has the following four types of steady-state solutions: (i) stripes of amplitude

$$R_1 = \sqrt{\frac{22}{(16\xi - 5)(7 - 8\xi)}}, \quad R_2 = 0,\ R_3 = 0, \tag{26}$$

or any circular permutation thereof; (ii) structures with hexagonal symmetry $R_1 = R_2 = R_3 = R$, where

$$R = \frac{253|16\xi - 17| + \sqrt{-51\,137\,119 + 173\,019\,616\xi - 127\,139\,584\xi^2}}{-34\,405 + 102\,688\xi - 70\,912\xi^2}; \tag{27}$$

(iii) mixed states in which two of three amplitudes are not equal to zero and one is equal to zero; and (iv) flat state $R_1 = R_2 = R_3 = 0$.

Solutions (ii) and (iv) are unstable for any value of ξ. The relative stability of solutions (i) and (ii) can be determined by linearization of the system of equations (25) about both the stripes and hexagonal hill solutions. The eigenvalues of the resulting Jacobian were defined analytically. The results show that the stripe solution can exist for $\xi \in (0.32, 0.88)$ and the hexagon solution can exist for $\xi \in (0.53, 0.92)$. However, the stripe solution is stable only for $\xi \in (0.68, 0.88)$ and the hexagonal solution is stable for $\xi \in (0.57, 0.88)$. That regular patterns do not exist for $\xi < 0.57$ and $\xi > 0.88$ is consistent with our experimental data. (The parameter ξ will be shown to decrease with voltage.) That the regular patterns appear only within a small window near $\xi = 1$ is also consistent with our earlier speculation. However, that stable hexagons and stripes coexist for $0.68 < \xi < 0.88$ requires further analysis. We computed the eigenvectors of all the steady states for $0.57 < \xi < 0.68$ and $0.68 < \xi < 0.88$. These eigenvectors allow us to decipher the direction of the trajectory along heteroclinic connections between the steady states. As seen in Fig. 6, we find all initial conditions near the origin (flat state) to evolve first towards a stripe pattern along the unstable eigenvector of the origin in both regions, regardless of the stability of the stripe. In the first region, the stripe is unstable and the trajectory comes close to it but then departs along its unstable eigenvector towards the stable hexagon. This near miss corresponds to how the stripes break up into hexagonal hill patterns. In the second region, however, the trajectory stays with the stable stripe pattern and never approaches the hexagon despite the latter's stability. Although the heteroclinic connections are actually stable and unstable manifolds,[20] the eigenvectors yield simple and accurate approximations of them. They indicate that if the anode is almost uniformly flat initially, stripes will be selected for $\xi \in (0.68, 0.88)$, while hexagons will be the final selected state for $\xi \in (0.57, 0.68)$.

Actually, the above bifurcation analysis only indicates that regular stripe patterns are expected within the window $\xi \in (0.68, 0.88)$ and the hexagonal patterns within $\xi \in (0.57, 0.68)$. Since we have subjected the patterns to noise from only certain discrete modes, it is not clear if they will remain stable in the presence of more wideband noise. It also does not indicate which patterns will exist outside the window $\xi \in (0.57, 0.88)$, although they certainly cannot be periodic states. We answer both questions by carrying out a numerical simulation of Eq. (16). We use a finite-difference numerical scheme with a grid size of 0.589 and a time step of $\Delta\tau = 10^{-3}$. Computations are done for $\xi = 0.8842$, $\xi = 0.7664$, $\xi = 0.6235$, and $\xi = 0.4733$. (These strange numbers will be shown to correspond to convenient voltages.) The computation domain is large enough to contain eight wavelengths of the fastest mode q_m. Small random deviations were adopted as initial conditions.

It is quite clear from the snapshots shown in Fig. 7 that no regular structure appears for $\xi = 0.8842$. Instead, the average separation tends to increase, while contorted stripes tend to persist. Although regularly spaced stripes are not possible, isolated hills still tend to connect and form randomly oriented stripes. For $\xi = 0.7664$ in Fig. 8, the hills also reconnect to form stripes, but the latter now strive to stretch and form regular patterns by expelling any remaining defect. There is also no coarsening trend that increases the average

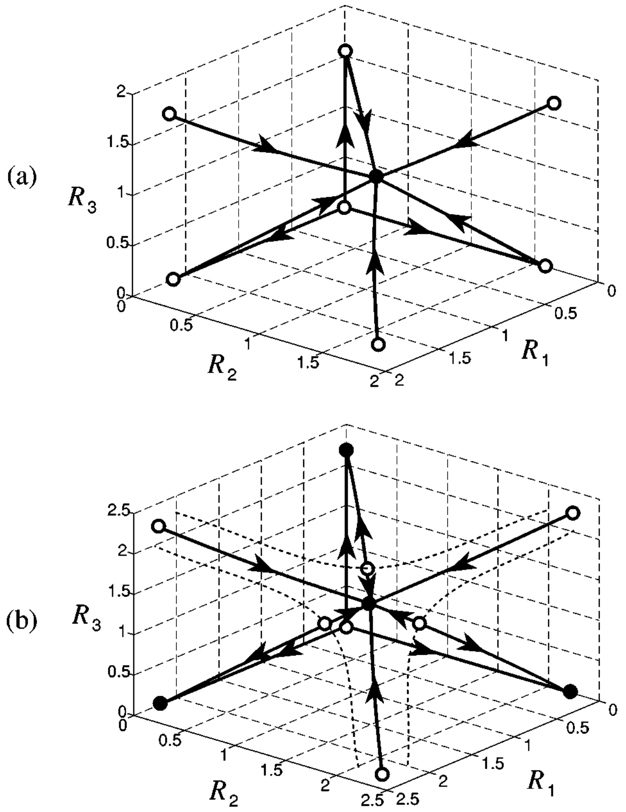

FIG. 6. Phase-space trajectories for (a) $0.57 < \xi < 0.68$ and (b) $0.68 < \xi < 0.88$. The origin is the unstable planar interface, fixed points on the axes are stripe patterns, the fixed point in the middle is the hexagonal patterns, and unstable mixed patterns also appear in (b).

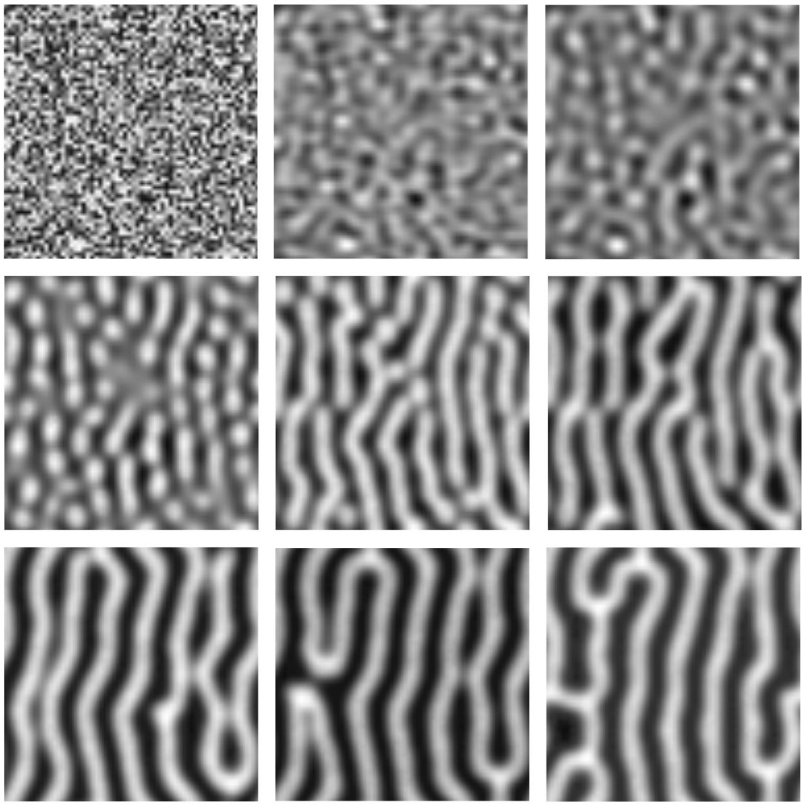

FIG. 7. Numerical simulations of the electrode surface evolution from random initial conditions at $\xi=0.8842$ (40 V).

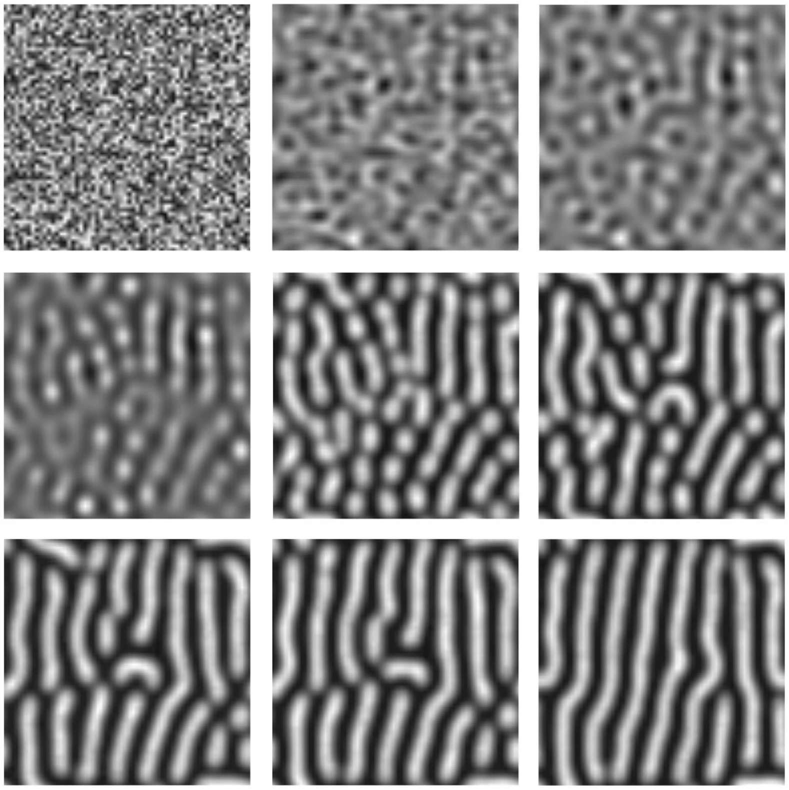

FIG. 8. Numerical simulations of the electrode surface evolution from random initial conditions at $\xi=0.7664$ (50 V).

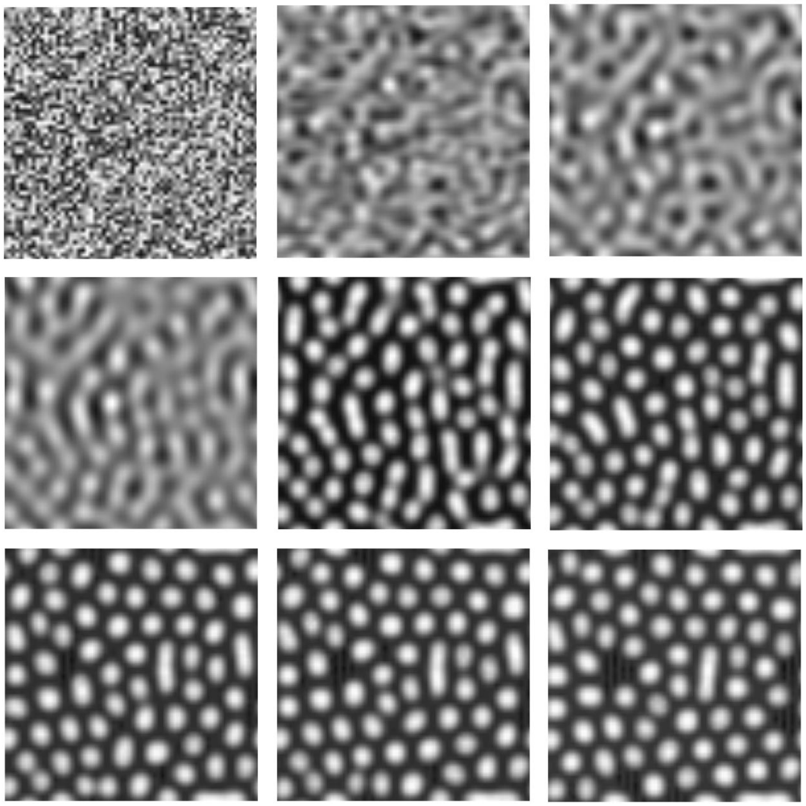

FIG. 9. Numerical simulations of the electrode surface evolution from random initial conditions at $\xi = 0.6235$ (60 V).

length scale. Such late-stage stretching dynamics towards regular stripe patterns is extremely slow and some defects remain at $\tau = 2000$. For $\xi = 0.6235$ (Fig. 9) when we expect regular hexagons, the initial dots do not connect and instead tend to form randomly symmetric hills. These hills also seem to strive to form regular hexagonal patterns with a very slow dynamics. Finally, for $\xi = 0.4733$ (Fig. 10), the disconnected dots are much more irregular, while stripe patterns are missing entirely.

While we clearly see tendencies to form isolated hills at small ξ and longer stripes at large ξ, the formation of regular stripes and hexagons at the intermediate windows in ξ, as suggested by the bifurcation analysis, is not clear from the above simulations with random initial conditions. To remedy this, we accelerate the long-time dynamics by using random initial conditions only within a narrow strip while the remaining domain is initially smooth. As is evident in Figs. 11 and 12, regular straight stripe patterns propagate away from this strip. These stripes survive for $\xi = 0.7664$ and break up into perfect hexagonal hills for $\xi = 0.6235$. Such a selection of regular patterns from a propagating front has been seen in other systems.[23] Although we have exploited this phenomenon here to expedite the pattern formation process, it may in fact happen in the actual electropolishing process if the dominant noise source for the microscopic dynamics is from the intersection of crystal defects with the surface that produce straight boundaries (slip lines, twin boundaries, etc.). Such slip steps distort the double-layer thickness and trigger nonuniform dissolution along the straight domain wall. The resulting patterns will then resemble those in Figs. 11 and 12. Finally, cross-section profiles of the regular stripes and patterns from our simulations in Figs. 11 and 12 are compared in Fig. 13 to the measured ones obtained from the AFM images in Figs. 2(b) and 2(c). Careful analysis of the obtained profiles shows the presence of the sharp crests that we have attributed earlier to the enhanced dissolution at the nodes for $\nu < 1$.

IV. COMPARISON WITH EXPERIMENTAL DATA

To actually obtain quantitative prediction for the measured wavelength and voltage windows for the various patterns in Fig. 4, we need to relate ξ and ν to the applied voltage with some reasonable approximations. Given the complexity of the adsorption-desorption and diffusion processes and the lack of knowledge about them, some assumptions are necessary, but we shall be careful to invoke only the most reasonable and least crucial ones. From these definitions

$$\nu(E_0) = \frac{\beta_r}{2\alpha E_0 K_a^0(E_0)},$$

$$\xi = \frac{\delta_E^2}{8\nu}\left(\frac{k_d^0}{D_s^0}\right)\left(\frac{\alpha E_0^2}{k_B T} + 1\right), \tag{28}$$

where $K_a^0(E_0)$ is the adsorption-desorption equilibrium constant at E_0 defined in Eq. (11) and the reference diffusion length scale of the shielding molecule $\ell_D = (D_s^0/k_d^0)^{1/2}$ is also a function of E_0.

We first relate the planar electric field to the voltage applied to the electropolishing cell U by assuming that $\Delta\psi_H$ is negligible and there is a double layer of equal thickness at the cathode such that

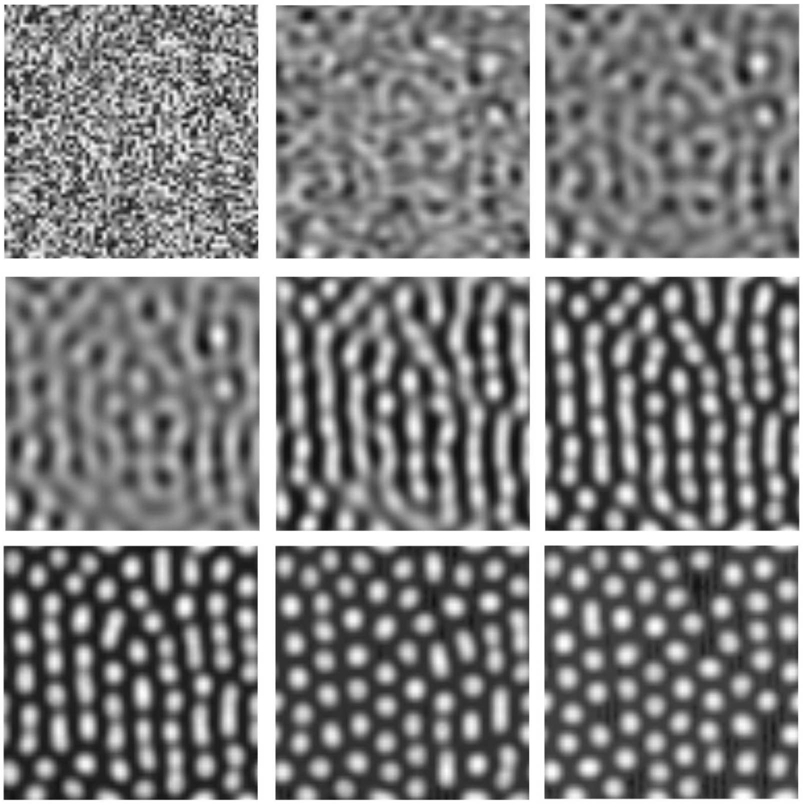

FIG. 10. Numerical simulations of the electrode surface evolution from random initial conditions at ξ=0.4733 (70 V).

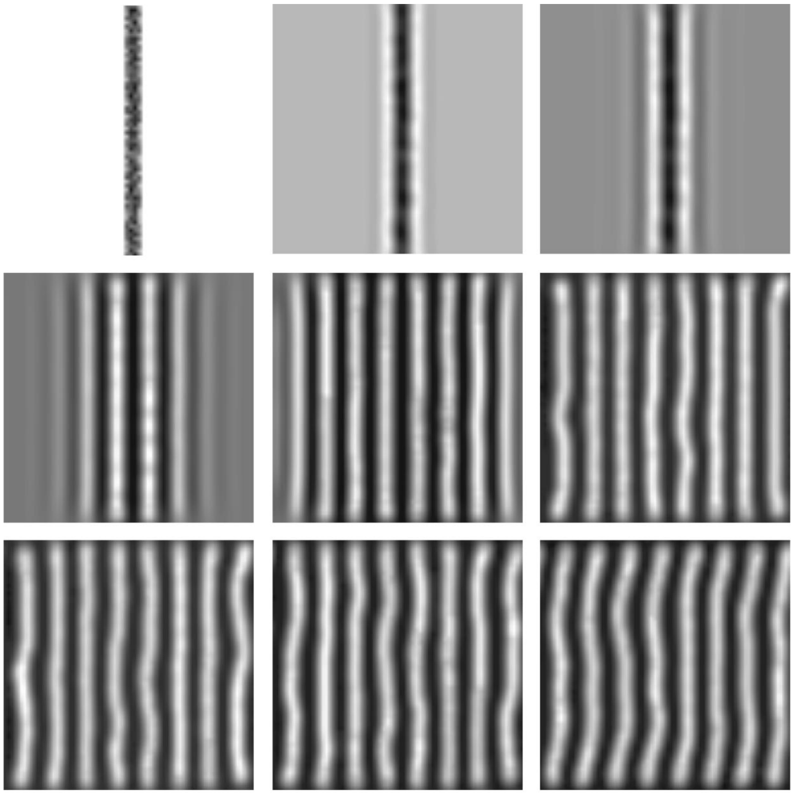

FIG. 11. Numerical simulations of the electrode surface evolution from a domain boundary at ξ=0.7664 (50 V).

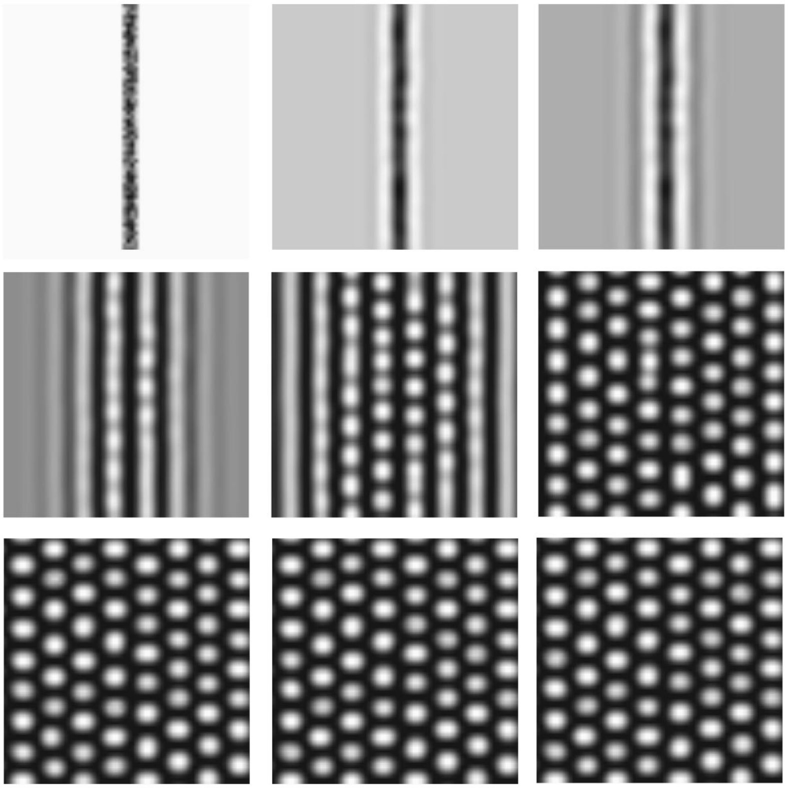

FIG. 12. Numerical simulations of the electrode surface evolution from a domain boundary at $\xi = 0.6235$ (60 V).

$$E_0 = \frac{U}{2\delta_E}. \tag{29}$$

This should be a good approximation with only some error in the factor 2, which does not affect the voltage dependence. We then assume that the adsorption, desorption, and surface diffusion are activated processes with a common transition state. This is not unreasonable if the diffusing shielding molecule has to hop through the bulk to reach a different location on the surface. We shall also assume, as before in Eq. (9), that this transition state of the shielding molecule has nearly the same dipole moment as other polar molecules that compete for the surface such that only the energy of the induced dipole moment αE_0^2 appears in the activation energy. However, unlike $k_a(E_0)$ in Eq. (9), we expect $k_d^0(E_0)$ and $D_s^0(E_0)$ to have activation energies that scale as $-E_0^2$ instead of $+E_0^2$. From Fig. 4, however, the length scale $(D_s^0/k_d^0)^{1/2}$ must increase with voltage. This will occur only if the activation energy of k_d^0 is larger in magnitude than that of D_s^0. This then yields

$$\frac{D_S^0}{k_d^0} = \frac{D_S^*}{k_d^*}\exp\left(\beta\frac{\alpha E_0^2}{k_B T}\right) = \frac{D_S^*}{k_d^*}\exp\left(\beta\frac{\alpha U^2}{4\delta_E^2 k_B T}\right), \tag{30}$$

where β is a positive coefficient of unit order. We also use Eq. (9) to rewrite ν as

$$\nu = \frac{\beta_r \delta_E}{\alpha U K_a^*}\exp\left(-\frac{\alpha U^2}{8\delta_E^2 k_B T}\right). \tag{31}$$

The difference in polarizability between the shielding molecule and water α was already estimated to be 4.7×10^{-40} J/(V/m)^2 in Eq. (9). The coefficient β is a unit order quantity and will be set directly to one without significant loss of information. For δ_E, we use a reasonable and convenient value of 10 nm for dilute electrolytes. The coefficient β_r for most field-assisted metal dissolution is estimated[18] to be 3.7×10^{-31} J/(V/m). These assignments would completely specify ν in Eq. (31) if the fieldless adsorption-desorption equilibrium constant K_a^* is known. Specification of the fieldless diffusion length $(D_S^*/k_d^*)^{1/2}$ in addition to K_a^* would also specify ξ. Hence ν and ξ are now dependent on two parameters K_a^* and D_S^*/k_d^*. We note that the dissolution rate K_r^0 is not required if we are not concerned with the time scale. In any case, K_r^0 is measurable from the current.

In dimensional variables, the wavelength of fastest growing mode with dimensionless wave number

$$q_m = \sqrt{\frac{\sqrt{\nu}}{1+\sqrt{\nu}}}$$

of Eq. (20) is

$$\begin{aligned}\ell(U) &= 2\pi\sqrt{\frac{D_S^0}{k_d^0}}\sqrt{\frac{\sqrt{\nu}}{1-\sqrt{\nu}}}\\ &= 2\pi\sqrt{\frac{\sqrt{\nu}}{1-\sqrt{\nu}}}\sqrt{\frac{D_S^*}{k_d^*}\exp\left(\frac{\alpha U^2}{4\delta_E^2 k_B T}\right)}.\end{aligned} \tag{32}$$

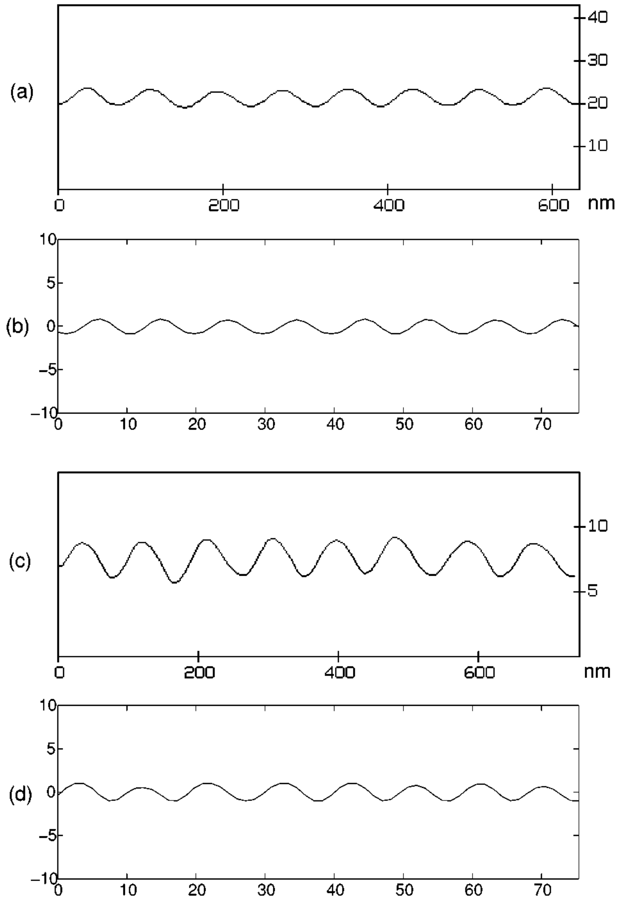

FIG. 13. Comparison of the profiles for (a) and (b) the stripe pattern with (c) and (d) profiles for the regular hexagon pattern obtained from (a) and (c) AFM data and (b) and (d) numerical simulations.

Since the wavelength in the limit of zero voltage $\ell(0)=55$ nm can be estimated by extrapolating the data in Fig. 4, this provides an additional condition and reduces the degree of freedom to a single one K_a^*.

We hence adjust K_a^* until Eq. (32) can satisfactorily fit the wavelength data. Due to the scatter in Eq. (32), a wide range of K_a^* seems to yield a satisfactory fit. We choose a convenient value of $K_a^*=1/3$. While we can find no literature value for the adsorption-desorption equilibrium constant for our molecules on Al, this value is quite comparable to the reported value of ethanol on silica gel.[24]

With the given value of K_a^*, $\nu(U)$ in Eq. (31) is completely specified and is plotted in Fig. 14. Note that there exists a threshold voltage at $U_{c1}=22.7$ V for pattern formation when $\nu=1$. We are unable to polish our anode at such a low voltage and hence could not verify this onset voltage. However, the experimental data for high voltages is consistent with the value of the upper critical voltage $U_{c2}=67.5$ V ($\nu=1/4$), where the resonant modes $\hat{V}_j$ lose their stability and hence the patterns become nonregular. We observe, however, that ν remains in the range (0.3, 0.8) for the pertinent range from 30 V to 60 V. We hence choose the convenient value of $\nu=0.64$ indicated in Sec. III. The final results for wavelength and voltage windows are off by no more than 10% by changing this value by 0.1.

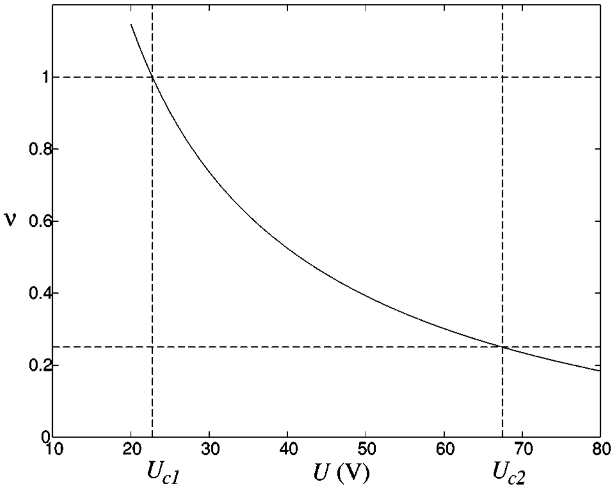

FIG. 14. Dependence of the parameter ν on the applied voltage U; the lower critical voltage $U_{c1}=22.7$ V and the upper critical voltage $U_{c2}=67.5$ V.

This convenient ν value then offers compact expressions for all the pertinent quantities

$$\sqrt{D_S^*/k_d^*}=4.33\ \text{nm}, \tag{33}$$

$$\ell(U)=4\pi\sqrt{D_S^*/k_d^*}\exp\left(\frac{\alpha U^2}{4\delta_E^2 k_B T}\right), \tag{34}$$

$$\xi=(1.04+3.07\times10^{-4}U^2)\exp(-3.43\times10^{-4}U^2), \tag{35}$$

where U is the applied voltage (in volts), α is estimated in Eq. (9), and δ_E is taken to be 10 nm. These estimates are quite consistent with typical measured values. For example, recent measurements for n alkanes on Ru(001) in vacuum yield an extrapolated value of $\sqrt{D_S^*/k_d^*}=4.84$ nm for methane.[25] The fieldless diffusion length of 4.33 nm, corresponding to the measured wavelength $\ell(0)$ of 55 nm in Fig. 4, is hence reasonable.

The curve in Fig. 4 is drawn from Eq. (34), which was obtained by adjusting only a single model parameter K_a^*. A more stringent test is the prediction of the voltage windows where regular stripes and hexagonal hills are predicted. From Eq. (35), since ξ decreases with increasing U, the window for stripes $(0.68<\xi<0.88)$ now corresponds to 40.4 V$<U<$56.2 V, while the window for hexagonal hills $(0.57<\xi<0.68)$ now lies in the range 56.2 V$<U<$63.4 V. These predicted windows are also shown in Fig. 4 and they are in excellent agreement with the observed patterns. It is a testimony to the robustness and accuracy of the model that one single adjustable parameter can provide such accurate predictions of not only the length scale but also the patterns as functions of the applied voltage. The ξ values (0.8842, 0.7664, 0.6235, and 0.4733) in the simulations correspond to whole-figure voltages (40, 50, 60, and 70) in the various pattern windows. As seen before, the simulation not only produces periodic stripes and hexagons in the proper windows but also shows random stripes at low voltage and random hills at high voltage. We have not attempted to model or measure $K_r^0(E_0)$ to also specify the actual times each pattern appears in a particular experiment. Nevertheless, our measured current value at 60 V indicates K_r^0 (60 V)$\sim$0.4 μm/sec. This translates the dimensionless time $\tau=500$ for the middle snapshot in the bottom row in Figs. 9–12 to approximately $t=60$ sec, which is consistent with the observed transition times in Fig. 1. A more detailed correlation is not attempted due to the ambiguity about the actual initial condition. The wavelength and voltage-dependent pattern selection are, however, dependent only on the activation energy of K_r^0 and not the actual dissolution rate. Knowledge about ξ and ν completely specifies the evolution, but not the time scale.

V. DISCUSSION

The most attractive application of the periodic stripe and hexagonal hill patterns, like self-assembly of regular surface micelle patterns by surfactants, is to use them to manufacture nanoelectronic functional devices. However, Al itself does not serve this purpose and one can only hope to use the Al patterns as templates for other materials. For this reason, it is better to develop patterns on Zr since anodization of any metal surface with the hexagonal hills has been observed to produce a porous oxide film with a highly regimented array of deep pores[26] and zirconia film is a much better substrate than porous alumina.[27] Our preliminary electropolishing experiments of Zr coupons shown in Fig. 15 show the same pattern dependence on voltage as Al, but we have yet to pinpoint the voltage window for regular hexagons. If ν is close to zero, it is quite conceivable that such a window cannot be reached with the same electrolyte. However, it does look like the same coupling between the diffusion of a shielding molecule with interfacial curvature and tension (stretching) is a general mechanism for pattern formation during electropolishing. We intend to use our current theory to design the most desirable patterns for any metal by altering the electrolyte composition, which changes the adsorption, desorption, and diffusion rates and the Debye thickness δ_E and by adjusting the temperature and voltage.

ACKNOWLEDGMENTS

Several colleagues in our laboratory have contributed to this effort. D.-F. Yue[28] first observed the patterns reported here and we benefited from discussions with O. Orlichenko, A. Indeikina, and G. Banerjee. K. Krischer from Fritz-Haber-Institut der Max-Planck-Gessellschaft pointed out the role of the Helmholtz layer. H.-C.C. was partially supported by the NSF, Grant No. CTS95-22277. V.V.Y. and A.E.M. acknowledge financial support from the Midwest Superconductivity Consortium, MISCON (DOE Contract No. DE-FG02-90ER45427). We are also grateful to Professor E. E. Wolf for the use of an AFM purchased with NSF funds.

APPENDIX: LONG-WAVELENGTH EXPANSION OF THE POISSON EQUATION

Since the characteristic interfacial amplitude is δ_E while the characteristic wavelength ℓ is much longer than δ_E, we use the scaling

$$\overline{(x,y)}=(x,y)/\ell,$$

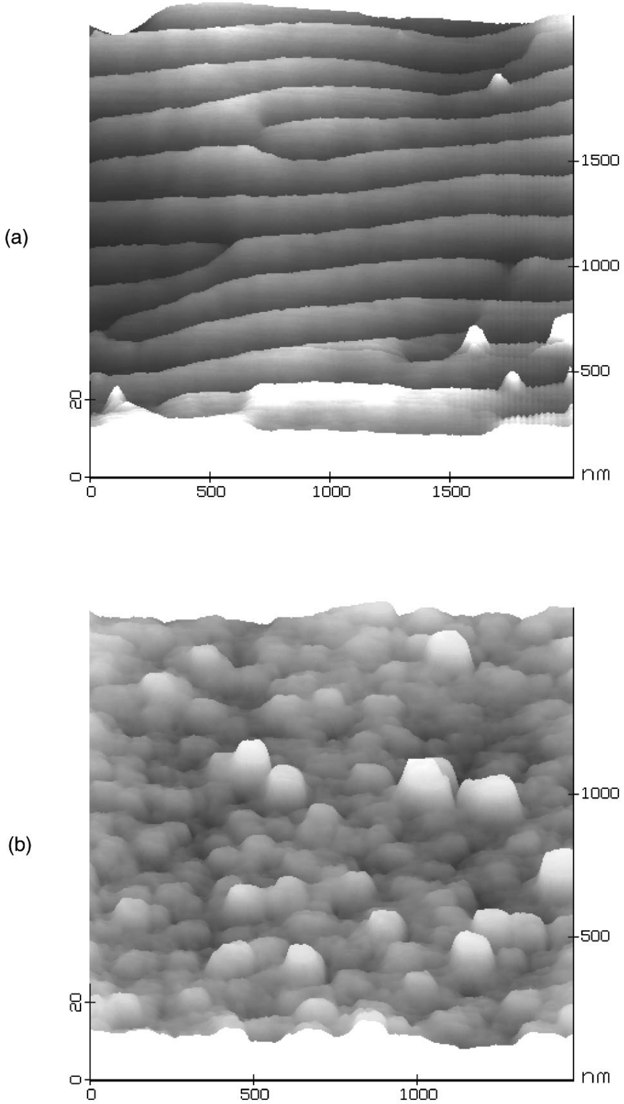

FIG. 15. AFM images of the surface patterns on zirconium that was electropolished at (a) 60 V and (b) 70 V.

$$\overline{z}=z/\delta_E,$$

$$\overline{h}=h/\delta_E$$

to normalize Eq. (1) to

$$\frac{\partial^2\psi}{\partial\overline{z}^2}+\varepsilon^2\left(\frac{\partial^2\psi}{\partial\overline{x}^2}+\frac{\partial^2\psi}{\partial\overline{y}^2}\right)=\psi,$$

$$\psi|_{\overline{z}=\overline{h}}=\psi_s,$$

$$\psi|_{\overline{z}\to\infty}=0.$$

Expanding ψ in the long-wavelength parameter $\varepsilon=\delta_E/\ell\ll 1$, $\psi\approx\psi^0+\varepsilon^2\psi^1$, we obtain for $O(\varepsilon^0)$

$$\frac{\partial^2\psi^0}{\partial\overline{z}^2}=\psi^0,$$

$$\psi^0|_{\overline{z}=\overline{h}}=\psi_s,$$

$$\psi^0|_{\overline{z}\to\infty}=0.$$

Note that this ψ^0 is distinct from ψ_0 in the text, which is strictly for the planar geometry. This leading-order equation can be solved to yield

$$\psi^0=\psi_s \exp(\overline{h}-\overline{z}),$$

where $\overline{h}=\overline{h}(\overline{x},\overline{y})$.

Continue to the next nontrivial $O(\varepsilon^2)$; we obtain

$$\frac{\partial^2\psi^1}{\partial \overline{z}^2}=-\overline{\nabla}^2\psi^0+\psi^1,$$

$$\psi^1|_{\overline{z}=\overline{h}}=0,$$

$$\psi^1|_{\overline{z}\to\infty}=0,$$

where

$$\overline{\nabla}^2\psi^0=\left(\frac{\partial^2}{\partial\overline{x}^2}+\frac{\partial^2}{\partial\overline{y}^2}\right)\psi^0$$

$$=\psi_s \exp(\overline{h}-\overline{z})[(\overline{\nabla h})^2+\overline{\nabla}^2\overline{h}].$$

The first term in the square brackets denotes a line stretching term that arises when the Poisson equation is perturbed, when Laplacian is operated on the leading-order field ψ^0 that has an exponential dependence on the interfacial position $\overline{h}$.

The next-order field term ψ^1 can also be readily obtained,

$$\psi^1=\frac{\psi_s}{2}(\overline{z}-\overline{h})\exp(\overline{h}-2\overline{z})[(\overline{\nabla h})^2+\overline{\nabla}^2\overline{h}].$$

Hence the field is given by

$$\overline{E}\approx-\left.\frac{\partial\psi}{\partial\overline{z}}\right|_{\overline{z}=\overline{h}}\approx-\left.\frac{\partial\psi^0}{\partial\overline{z}}\right|_{\overline{z}=\overline{h}}-\varepsilon^2\left.\frac{\partial\psi^1}{\partial\overline{z}}\right|_{\overline{z}=\overline{h}}=\overline{E}_0+\overline{E}_1$$

and hence

$$\overline{E}_0=\psi_s,$$

$$\overline{E}_1=-\varepsilon^2\frac{\psi_s}{2}[(\overline{\nabla h})^2+\overline{\nabla}^2\overline{h}].$$

Since ℓ is unspecified, we need to return to the unscaled variables to yield

$$E_1=-\frac{E_0}{2}[(\nabla h)^2+\delta_E\nabla^2 h],$$

which is the deviation field due to interfacial variation from the flat geometry in Eq. (5) with the signature stretching and curvature terms.

---

*Author to whom correspondence should be addressed.

[1] D. M. Kolb, Prog. Surf. Sci. **51**, 109 (1996).

[2] S. Manne and H. E. Gaub, Science **270**, 1480 (1995).

[3] J. O. Bockris, M. A. Devanathan, and K. Muller, Proc. R. Soc. London, Ser. A **274**, 55 (1963).

[4] D. M. Kolb, J. Vac. Sci. Technol. A **4**, 1294 (1986).

[5] G. Flätgen and K. Krischer, J. Chem. Phys. **103**, 5428 (1995).

[6] G. Flätgen *et al.*, Science **269**, 668 (1995).

[7] C. A. Miller and P. Neogi, *Interfacial Phenomena* (Dekker, New York, 1985).

[8] V. G. Levich, *Physicochemical Hydrodynamics* (Prentice-Hall, Englewood Cliffs, NJ, 1962).

[9] C. Barnes, Trans. IMF **63**, 52 (1985).

[10] C. Wagner, J. Electrochem. Soc. **101**, 225 (1954).

[11] R. Vidal and A. C. West, J. Electrochem. Soc. **142**, 2682 (1995).

[12] W. W. Mullins and R. F. Skerka, J. Appl. Phys. **35**, 444 (1964).

[13] N. C. Welsh, J. Inst. Met. **85**, 129 (1956).

[14] M. Pourbaix, *Atlas of Electrochemical Equilibria in Aqueous Solutions* (NACE, Houston, TX, 1974).

[15] J. Goodisman, *Electrochemistry: Theoretical Foundations* (Wiley, New York, 1987).

[16] M. Kardar, G. Parisi, and Y.-C. Zhang, Phys. Rev. Lett. **56**, 889 (1986).

[17] J. N. Israelachvili, *Intermolecular and Surface Forces* (Academic, London, 1985).

[18] D. A. Jones, *Principles and Prevention of Corrosion* (Prentice-Hall, Upper Saddle River, NJ, 1996).

[19] A.-L. Barabasi, Phys. Rev. Lett. **70**, 4102 (1993).

[20] P. Manneville, *Dissipative Structures and Weak Turbulence* (Academic, Boston, 1990).

[21] J. Carr, *Applications of Center Manifold Theory* (Springer, Berlin, 1981).

[22] M. Cheng and H.-C. Chang, Phys. Fluids A **4**, 505 (1992).

[23] W. van Saarloos, M. van Hecke, and R. Holyst, Phys. Rev. E **52**, 1773 (1995).

[24] D. R. Matayo and J. P. Wightman, J. Colloid Interface Sci. **44**, 162 (1973).

[25] J. L. Brand, M. V. Arena, A. A. Deckert, and S. M. George, J. Chem. Phys. **92**, 5136 (1990).

[26] S. Bandyopadhyay *et al.*, Nanotechnology **7**, 360 (1996).

[27] J. M. Phillips, J. Appl. Phys. **79**, 1829 (1996).

[28] D.-F. Yue, Ph.D. thesis, Notre Dame, 1995.